

LEXICON OF TOPOLOGICAL DEFECTS IN ^3He SUPERFLUIDS¹

V. B. ELTSOV² AND M. KRUSIUS
*Low Temperature Laboratory,
Helsinki University of Technology,
Box 2200, FIN-02015 HUT, Finland*

Defects in the multi-dimensional macroscopic quantum field of the ^3He superfluids are localized objects with a topological charge and are topologically stable. They include point-like objects, vortex lines, planar domain-wall-like structures, and 3-dimensional textures, which may or may not include singular points or lines. An inventory of illustrations is presented which concisely lists the different experimentally confirmed defect structures in the A and B phases of superfluid ^3He .

1. Quantum Fields in ^3He superfluids

Experimental information on defect structures in quantum fields is fragmentary and restricted by the properties and constraints of each particular degenerate many-body system in which they are studied. A notable exception are the p-wave-paired ^3He superfluids. They provide a versatile laboratory system, with a multidimensional order parameter field, in which one can study objects of different dimensionality – point defects, quantized vortex lines, domain-wall-like topological solitons, and 3-dim textures. Some of these, like the point defects, have not yet been directly mapped, and their role remains elusive. Others on the other hand, have helped to illustrate general principles such as composite structure and topological confinement, nucleation, and interactions between objects of different topologies.

In addition to the diversity in structure, two more features have become important attributes of the current ^3He work. First, bulk superfluid ^3He is nearly devoid of extrinsic influence. The only weak heterogeneity is introduced by the surfaces of the containing vessel. Secondly, detailed theoretical understanding of the ^3He order parameter field exists [3] and can be effectively correlated with new experimental results. The latter originate to a large extent from noninvasive nuclear magnetic resonance measurement on the superfluid contained in a rotating cylinder.

Similar to the application of a magnetic field on a superconductor, rotation of a superfluid is the most effective means for modifying existing

structure in the order parameter field or for generating new structure, especially quantized vorticity. In the multi-dimensional order parameter field of the ^3He superfluids quantized vorticity can have different topology and structure. For instance, in the vortex core the order parameter may become singular or it may have a continuous singularity-free distribution. Altogether eight different types of vorticity have been discovered and described: one continuous structure in $^3\text{He-A1}$, three continuous structures and one singular in $^3\text{He-A2}$, and three singular ones in $^3\text{He-B}$. Theoretically many more structures have been proposed [4]. In practice however, the question how to form or nucleate a particular new defect structure often becomes the threshold which precludes experimental verification.

The investigation of the ^3He order parameter field can be characterized as “field theory in the laboratory”. Conceptual similarities exist between the symmetry-breaking phase transitions of ^3He and various other field theoretical models. This similarity extends far in the mathematical description of different phenomena [5]. Clearly the detailed properties of any one of these systems can only be worked out by studying each of them individually, with specific experimental input. However, in the very least comparative work on a model system, like the ^3He superfluids, will provide general guide lines. Besides such comparative studies will teach us what kind of new questions should be answered by an experimental ^3He program – questions, which perhaps normally would not be standard practice within condensed matter physics.

A comprehensive review on topological defects in the ^3He superfluids does not exist at present time [6]. Here an abbreviated “pocket book” is provided, consisting of illustrations, extended figure descriptions, and the relevant references for further information.

2. Archive of defects in ^3He superfluids

Figure 1. The phase diagram of the fermionic liquid ^3He phases is shown here as a function of temperature T and pressure P at zero external magnetic field H . The normal phase exists at temperatures larger than the superfluid transition temperature T_c and is the best example of a system described by the Landau fermi liquid theory. Superfluid ^3He was the first system identified to exhibit Cooper pairing in the framework of the Bardeen-Cooper-Schrieffer theory in non-s-wave states with a total spin $S = 1$ and orbital momentum $L = 1$. The two major superfluid phases are the axially anisotropic A phase at high pressures and the quasi-isotropic B phase at low temperatures.

In the B phase, with Cooper pairing in a state with total angular momentum $\mathbf{J} = \mathbf{L} + \mathbf{S} = 0$, vortex lines have similar topology as in the

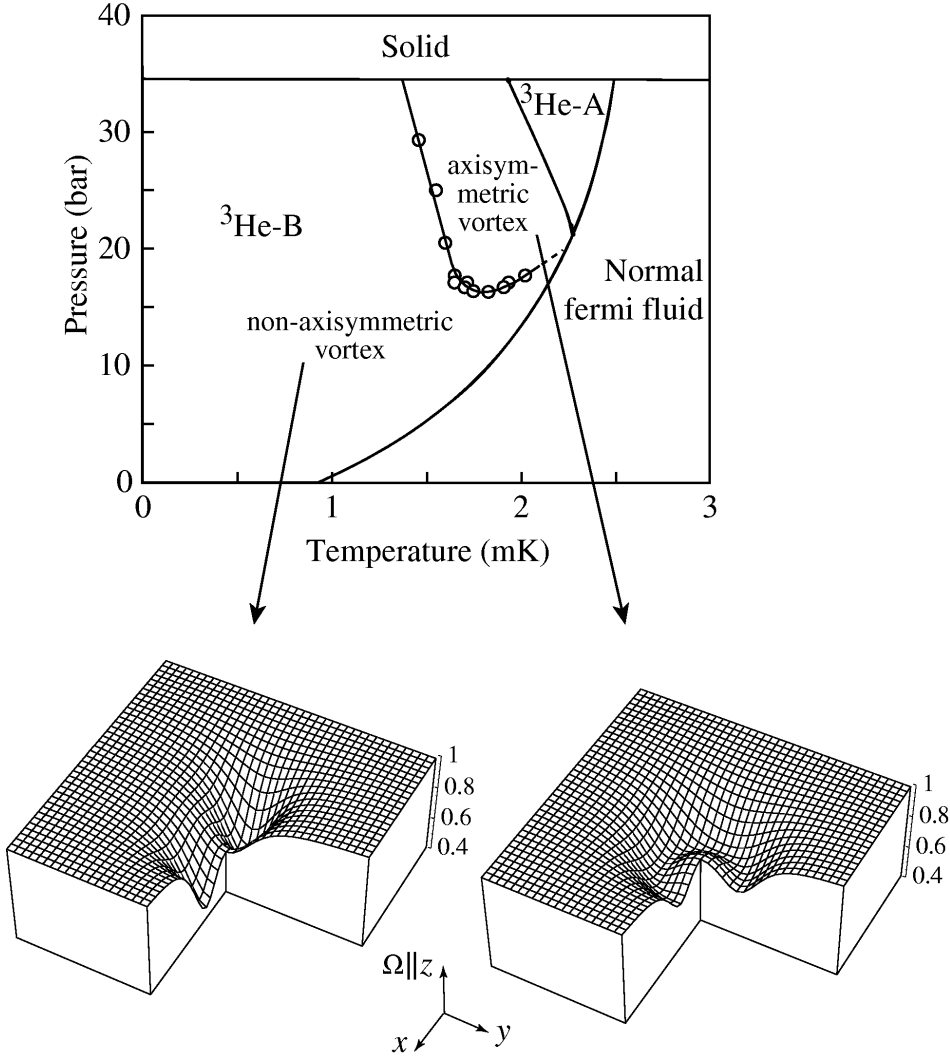


Figure 1. Phase transition in the singular core of B-phase vortices.

bosonic ⁴He superfluid and s-wave superconductors: a singular core which traps a phase winding by 2π around itself. The physical consequence from the trapped phase winding is a persistent superfluid current flowing around the core with a one-quantum circulation of $\kappa_0 = h/(2m_3) = 0.067 \text{ mm}^2/\text{s}$. Already the very first rotating experiments displayed a first order phase transition [7], which only could be explained as a change in the vortex-core structure. This transition is shown in the phase diagram as a line with data points within the B phase region. This was the first example ever of a phase

transition in a topologically stable quantized defect.

Quite surprisingly for an object associated with rotation, the core was later shown, both theoretically [8, 4] and experimentally [9], to undergo a spontaneous symmetry break from an axisymmetric to a double-core structure. The order parameter amplitude $|A_{ij}|$ does not vanish in the center of the core, but remains finite and becomes A-phase like in the axisymmetric case while additional components must be included in the case of the double core. The inserts below the phase diagram show the magnitude of the order parameter $\Sigma|A_{ij}|^2$ in the core [8], with the width of the area shown being about $1 \mu\text{m}$. The rotation axis $\vec{\Omega} \parallel \hat{z}$ is perpendicular to the xy plane and vorticity is nonzero only in the core region.

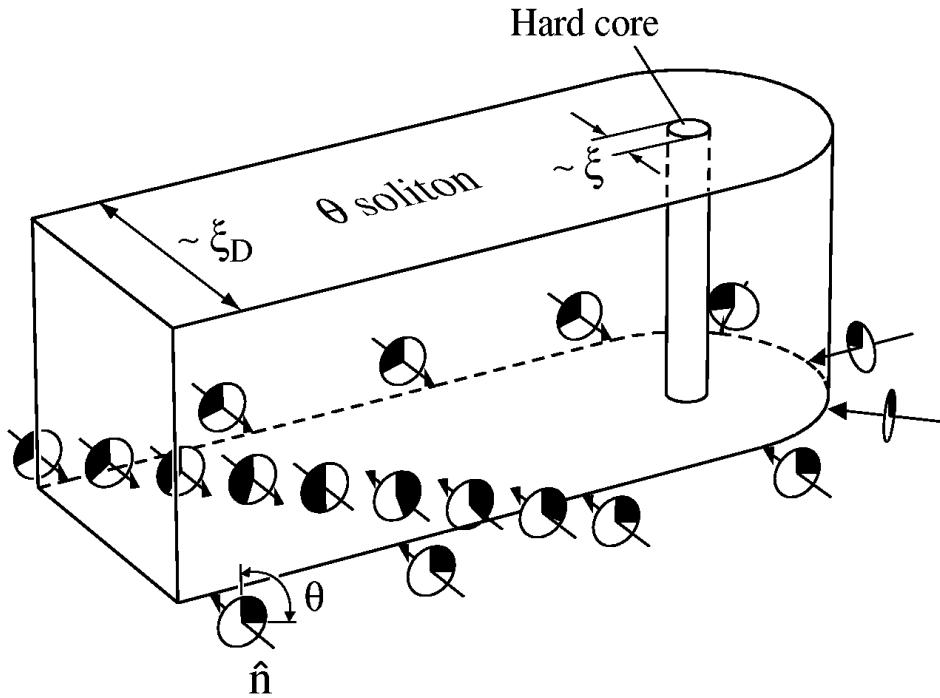


Figure 2. Spin-mass vortex in $^3\text{He-B}$.

Figure 2. The combined spin and mass current vortex in $^3\text{He-B}$ [10] is a composite object, consisting of a linear and a planar object. The singular vortex has here two functions: It is simultaneously a quantized vortex lines with a trapped supercurrent and an endline of a planar domain-wall-like topological soliton of the bulk texture. The two possible configurations are shown in Fig. 3, in which the spin-mass vortex can exist in the rotating container at finite external magnetic field.

The soliton is a defect in the spin-orbit interaction, ie. a wall within which the spin-orbit interaction is not minimized and which separates two degenerate regions with oppositely oriented B-phase textures ($H \neq 0$). In $^3\text{He-B}$ the relative orientation of the orbital and spin coordinate axes remains undefined as long as the minute spin-orbit interaction is not taken into account. To minimize the dipolar spin-orbit interaction the orbital and spin axes have to be rotated with respect to each other by an angle $\theta_L = \arccos(-\frac{1}{4}) \approx 104^\circ$. The rotation is generally specified in terms of a rotation matrix $R_{\alpha i}(\hat{\mathbf{n}}, \theta)$, where the unit vector $\hat{\mathbf{n}}$ gives the orientation of the rotation axis around which the rotation by θ_L is performed. Superfluid coherence, ie. the requirement to minimize the textural gradient energy, implies that the $\hat{\mathbf{n}}$ vector field becomes a smoothly varying texture in 3-dim space. The healing length for a defect in the $\hat{\mathbf{n}}$ texture is $\xi_D \sim 10 \mu\text{m}$, which thus is approximately the width of a textural soliton wall.

As depicted with arrows in the figure, $\hat{\mathbf{n}}$ is oriented perpendicular to the soliton wall in the bulk liquid and antiparallel on the opposite sides of the wall. Across the soliton θ traverses from θ_L to π in the center, where the orientation of $\hat{\mathbf{n}}$ reverses, and back to θ_L . On a path around the end of the soliton sheet $\hat{\mathbf{n}}$ smoothly changes orientation while θ remains fixed at θ_L .

The singular hard core has a radius comparable to the superfluid coherence length ξ which is typically 3 orders of magnitude smaller than the dipolar healing length ξ_D and the width of the θ soliton sheet. The core of the spin-mass vortex is a combination of two defects: 1) The winding of the superfluid phase factor by 2π around the core corresponds to a trapped superfluid circulation of one quantum κ_0 . This is the superfluid mass current. 2) The core is also a disclination line for the spin-orbit interaction with an accompanying trapped spin current. This is the spin current vortex.

Figure 3. The spin-mass vortex may be incorporated in a vortex cluster in the rotating container in two different configurations. A schematic cross-sectional cut transverse to the symmetry axis of the rotating cylinder is shown, with 5 spin-mass vortices in a vortex cluster. The usual mass current vortices are depicted with black dots while the spin-mass vortices correspond to the open circles. When the total number of vortex lines is less than the equilibrium value, then the existing lines are confined to a central vortex cluster which here is shown to have a radius R_v . The radius of the rotating container is R . The cluster is isolated from the cylinder wall by vortex-free counterflow, which as a function of the radial distance r has the velocity $v = v_s - v_n = -\Omega r(1 - R_v/r)$ within the counterflow annulus $R > r > R_v$ [11].

The spin-mass vortices are the edge lines for the θ solitons. The latter are marked in grey. A θ soliton can terminate either in a spin-mass vortex or on the cylinder wall. The two possible configurations for a spin-mass vortex

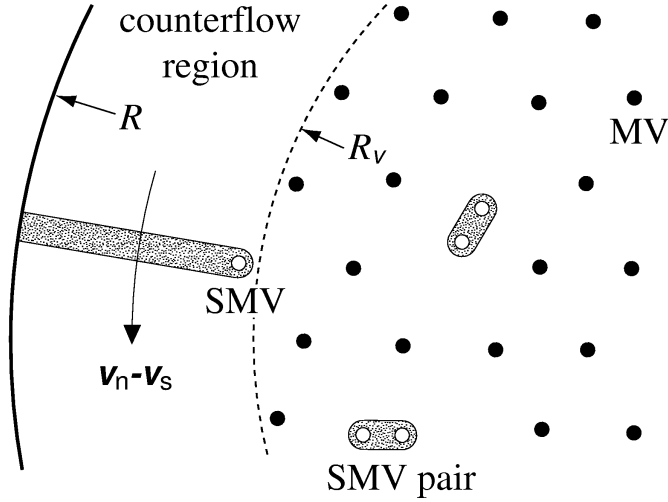


Figure 3. Spin-mass vortices in the rotating container with ${}^3\text{He-B}$.

are: 1) A soliton connects pairwise two spin-mass vortex lines which move to a distance d of each other where the soliton's surface tension σ balances the inter-vortex repulsion $F_M = \kappa_0^2 \rho_s / (2\pi d)$. This occurs at a distance $d = \kappa_0^2 \rho_s / (2\pi\sigma) \sim 6\xi_D$ which is generally somewhat less than the inter-vortex distance $2r_v \approx \sqrt{2\kappa_0 / (\pi\Omega)}$ between two mass-current vortices in a vortex array at usual experimentally accessible rotation velocities ($\Omega < 4$ rad/s). 2) A spin-mass vortex at the edge of the vortex cluster may have a soliton tail which connects to the cylinder wall. Compared to the Magnus force from the counterflow, $F_M = \kappa_0 \rho_s (v_s - v_n)$, the surface tension σ is small and therefore the spin-mass vortex lies close to the outer boundary of the vortex cluster. In this configuration the length of the soliton is maximized, it gives rise to larger changes in the NMR response, and can be more readily identified.

Figure 4. At T_c critical velocities vanish and the phase diagram of different vortex structures can be measured as a function of rotation velocity (Ω) and applied magnetic field (H) [12]. Each data point represents a rotational state which was obtained by cooling slowly from the normal phase to ${}^3\text{He-A}$ at a steady rotation velocity Ω in an applied magnetic field H . During the slow second order transition the equilibrium state at T_c is formed, with the equilibrium amount and the equilibrium structure of quantized vorticity.

Below T_c in the A phase the type of vortex lines was analyzed from the nuclear magnetic resonance spectra: White circles denote a state with only singly-quantized vortex lines which have a singular core. Their structure is

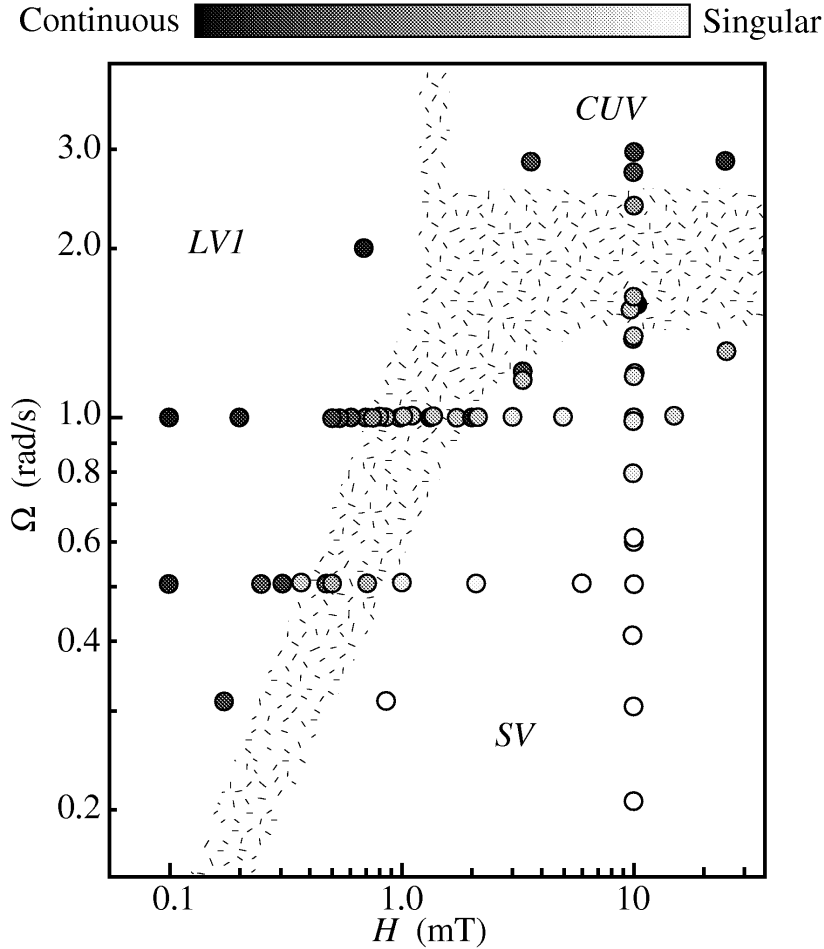


Figure 4. Measured phase diagram of different vortex structures in ${}^3\text{He-A}$ at T_c .

shown in Fig. 9. Black circles represent singularity-free vortex structures which at zero field are of the type shown in Fig. 7 and at high field as in Fig. 8. The degree of shading from white to black measures the relative amount of vorticity in the singularity-free structures.

The vertical phase boundary is the dipole locking \leftrightarrow unlocking transition, shown in more detail in Fig. 5. The horizontal boundary is the transition in the dipole-unlocked regime from the singly-quantized singular-core vortex (Fig. 9) at low $\Omega < 0.7$ rad/s to the singularity-free doubly-quantized vortex (Fig. 8) at large $\Omega > 1$ rad/s. The phase boundaries agree semi-quantitatively with the calculated phase diagram without adjustable parameters [13].

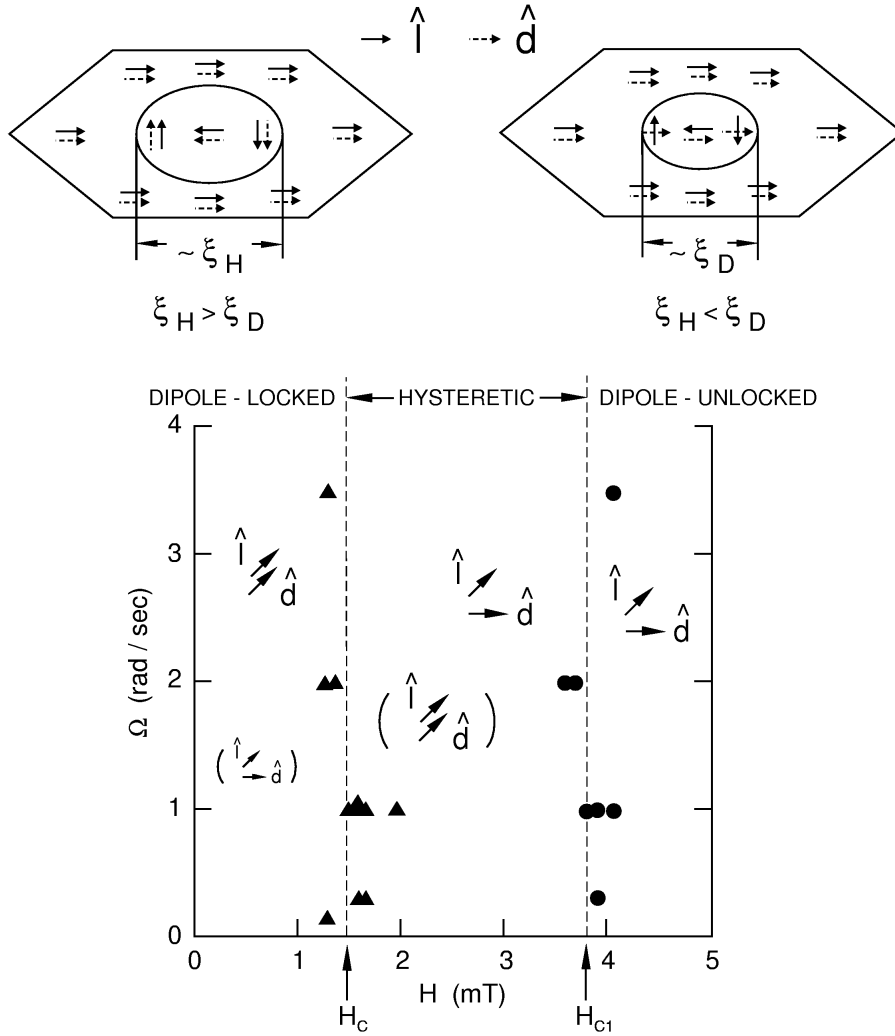


Figure 5. Topological dipole-locking \leftrightarrow unlocking transition in the A-phase vortex texture.

Figure 5. In $^3\text{He-A}$ a topological transition occurs in the vortex texture as a function of the applied magnetic field [14]. This dipole-locking \leftrightarrow unlocking transition takes place in the spatial orientational distribution of the spin quantization axis. The orientation of the spin axis is usually specified in terms of a unit vector $\hat{\mathbf{d}}$ which is oriented perpendicular to the spin \mathbf{S} . The orientation of the orbital quantization axis, in turn, is denoted with a unit vector $\hat{\ell}$ which points in the direction of the local orbital momentum \mathbf{L} . At low fields the dipolar spin-orbit interaction wins and orients $\hat{\mathbf{d}} \parallel \hat{\ell}$. This

is referred to as a *dipole-locked texture*. At high fields the coupling to the external field wins and orients $\hat{\mathbf{d}}$ uniformly perpendicular to \mathbf{H} while the orbital part is left to produce the vorticity. High-field textures are called *dipole unlocked*. The critical field for the dipole-locking \leftrightarrow unlocking transition is on the order of the dipolar field $H_D \sim 1$ mT at which the spin-orbit interaction equals the magnetic field anisotropy energy.

As illustrated schematically on the top, at high fields the dipole-unlocked texture is localized in the central part of the vortex, the so-called *soft vortex core*. Outside the soft core $\hat{\ell}$ is oriented uniformly parallel to $\hat{\mathbf{d}}$ (ie. $\hat{\ell} \parallel \hat{\mathbf{d}} \perp \mathbf{H}$). At low fields below the critical value H_c the uniform $\hat{\ell}$ texture is reduced in area and the central part with the inhomogeneous $\hat{\ell}$ texture increases, but now $\hat{\mathbf{d}}$ remains dipole locked to $\hat{\ell}$ even in this central region. Thus the dipole-locking \leftrightarrow unlocking transition separates two different topologies of the $\hat{\mathbf{d}}$ texture in the central part of the vortex. It is the dipole-unlocked part of the texture which leaves its distinct signature in the NMR spectrum and makes possible the NMR spectroscopy of order parameter defects in the A phase [15].

The low-field inhomogeneous $\hat{\mathbf{d}}$ texture is thus not stable as a function of the external field, but undergoes a first order phase transition. A measurement of this transition is shown in the main part of the figure in the rotation velocity (Ω) – applied magnetic field (H) plane. The different field regimes are denoted by the relative alignments of the $\hat{\mathbf{d}}$ and $\hat{\ell}$ vectors. Relative alignments in parenthesis denote a metastable field regime while without parenthesis the respective type of relative orientation is stable. The measured critical field $H_c(\Omega)$ is marked with triangles (\blacktriangle), while filled circles (\bullet) denote the catastrophe line $H_{c1}(\Omega)$ at which the low-field dipole-locked soft cores finally lose stability at the temperature $0.9 T_c$ of the measurements. At lower temperatures a distorted form of the dipole-locked vortex remains metastable to much higher fields: Below $0.6 T_c$ H_{c1} has been found to be more than 10 mT [15].

Figure 6. In $^3\text{He-A}$ the vortex texture in a rotating container is formed by the spatial variation in the orientation of the orbital quantization axis, the $\hat{\ell}$ vector field. Vorticity is nonzero, $\vec{\nabla} \times \mathbf{v}_s \neq 0$, in the regions where the $\hat{\ell}$ texture is inhomogeneous. The textures are continuous or singularity-free, if rotation is started in the A phase, because they have typically an order of magnitude lower critical velocity than a vortex with a singular core [16].

The extreme cases as a function of the applied magnetic field are: (*Bottom*) Zero-field periodic dipole-locked vortex texture. Here the nonuniform part of the $\hat{\ell}$ texture fills the entire vortex lattice cell. The dominant structure has a square lattice cell with 4 circulation quanta, as shown in Fig. 7. (*Top*) High-field ($H \gg H_D$) dipole-unlocked texture. Here the soft vortex core is formed and superficially the triangular vortex lattice starts to re-

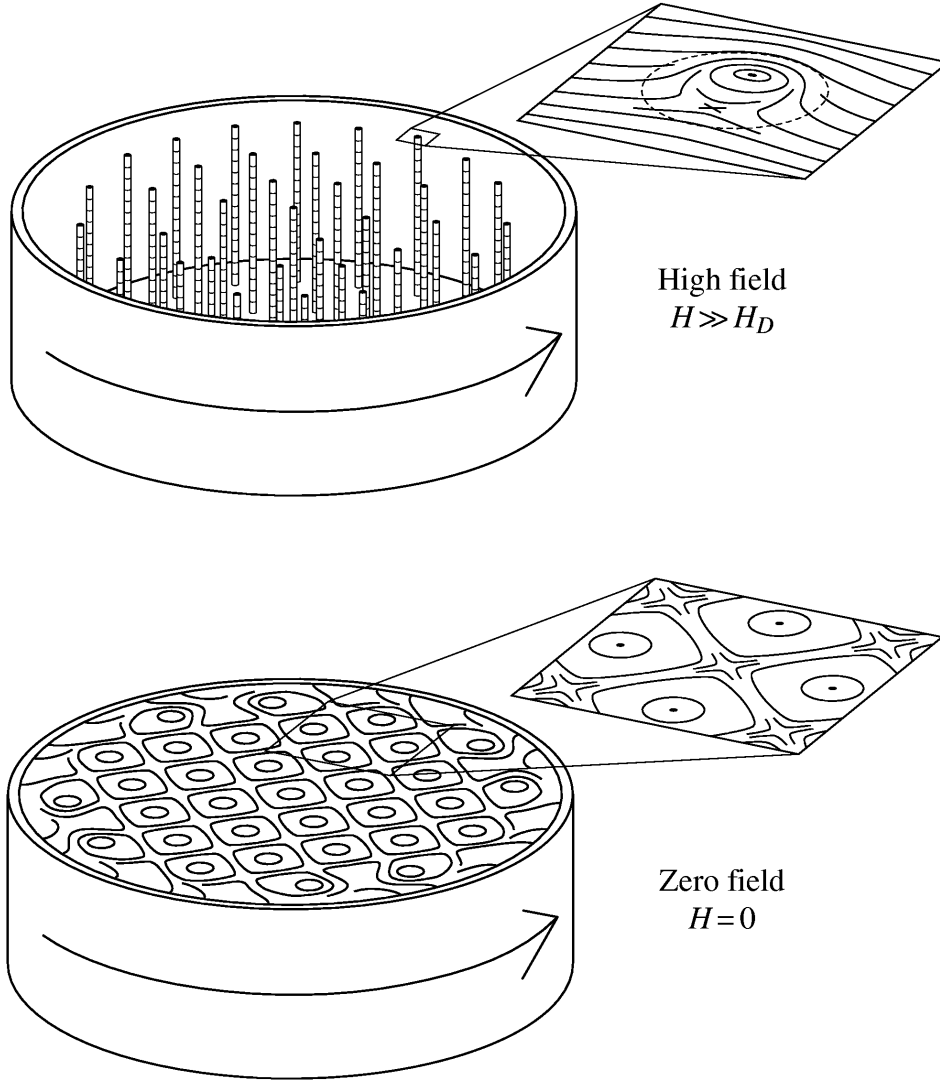


Figure 6. Rotating container with singularity-free vortex textures in ${}^3\text{He-A}$.

semble the more conventional case with singular vortex cores. Inside the soft core the $\hat{\ell}$ texture has the nonuniform and nonaxisymmetric structure shown in Fig. 8. The velocity v_s of the of the supercurrent increases smoothly from zero at the center of the soft core to a maximum at the edge. Outside the soft core the $\hat{\ell}$ texture is uniform, vorticity is zero, and the velocity of the persistent superflow decays with distance as $v_s = \kappa/(2\pi r)$, where $\kappa = 2\kappa_0 = h/m_3$ is the circulation trapped around the soft core.

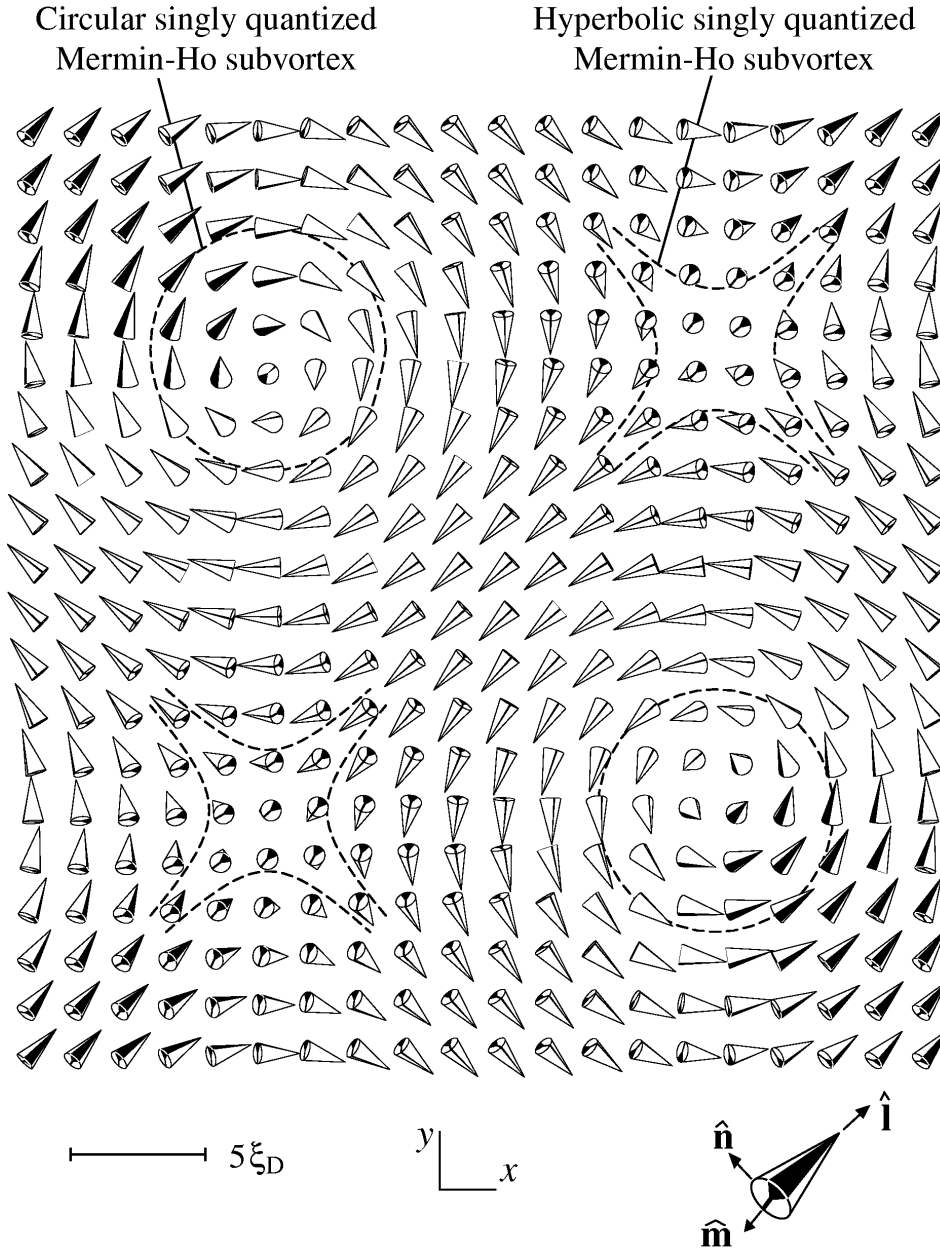


Figure 7. Orbital $\hat{\ell}$ texture of the dipole-locked vortex at zero external magnetic field in ${}^3\text{He-A}$.

Figure 7. The zero-field dipole-locked vortex in ${}^3\text{He-A}$ has a square elementary lattice cell with 4 circulation quanta [17, 13]. The figure shows

in the transverse xy plane (when $\hat{\mathbf{z}} \parallel \vec{\Omega}$) the orientation of the orbital unit vector triad $\hat{\ell} = \hat{\mathbf{m}} \times \hat{\mathbf{n}}$ within one vortex lattice cell. The yardstick gives the healing length ξ_D of the dipolar spin-orbit interaction relative to the gradient energy. Because of dipole locking $\hat{\ell}$ and $\hat{\mathbf{d}}$ have the same orientation everywhere. The viewing direction of this figure (and the following similar ones) is inclined by 14° from the z axis.

The texture is made up of 4 so-called Mermin-Ho vortices, two vortices with circular distribution of $\hat{\ell}$ orientations and two with hyperbolic. The boundaries of each of these 4 subunits is defined by the contours where $\hat{\ell}_z = 0$. A circular Mermin-Ho vortex includes all orientations of the positive unit hemisphere, where $\ell_z > 0$, and the hyperbolic vortex those of the negative hemisphere, where $\ell_z < 0$. Each of the Mermin-Ho vortices contributes one quantum of circulation to the total circulation of 4 quanta which is reached along the edge of the lattice cell. A stable configuration is attained with the pairwise antisymmetric arrangement in the square lattice. Other possibilities are a pairwise molecularization as in the dipole-unlocked high-field vortex (Fig. 8) or an alternating linear chain as in the vortex sheet (Fig. 12).

The above vortex texture has been derived from numerical minimization of the full textural free energy expression for an infinite bulk fluid with periodic boundary conditions at temperatures close to T_c [13]. At zero magnetic field the energy arises entirely from the gradient terms which are minimized when the orientational distribution over the lattice cell is as smooth as possible. When the magnetic field is switched on, the structure remains qualitatively unchanged, but the magnetic anisotropy energy attempts to reduce $|\hat{d}_z|$ and thus regions with large $|\hat{\ell}_z|$ values are squeezed closer to the center of the individual Mermin-Ho vortices at the expense of an increase in the gradient energy. The calculations show that at nonzero magnetic field also two other dipole-locked vortex textures have similar textural energies and may in fact become stable equilibrium states. One of them resembles a linear chain of circular and hyperbolic vortices, the dipole-locked variant of the vortex sheet, while the other is the dipole-locked molecule of a circular – hyperbolic pair in a triangular lattice [13]. Dipole-locking \leftrightarrow unlocking transitions are of first order because of the discontinuous change in the topology of the $\hat{\mathbf{d}}$ texture. They are experimentally easy to spot because of the associated textural hysteresis. In contrast, transitions between different dipole-locked textures would be weaker and harder to discern in the measurement.

Figure 8. The doubly-quantized high-field vortex in $^3\text{He-A}$ [18, 13] has a nonaxisymmetric soft core which consists of a circular – hyperbolic pair of Mermin-Ho vortices. Together these two include all 4π orientations of $\hat{\ell}$ within a unit sphere. This is seen by following the rotation of $\hat{\mathbf{m}}$ and

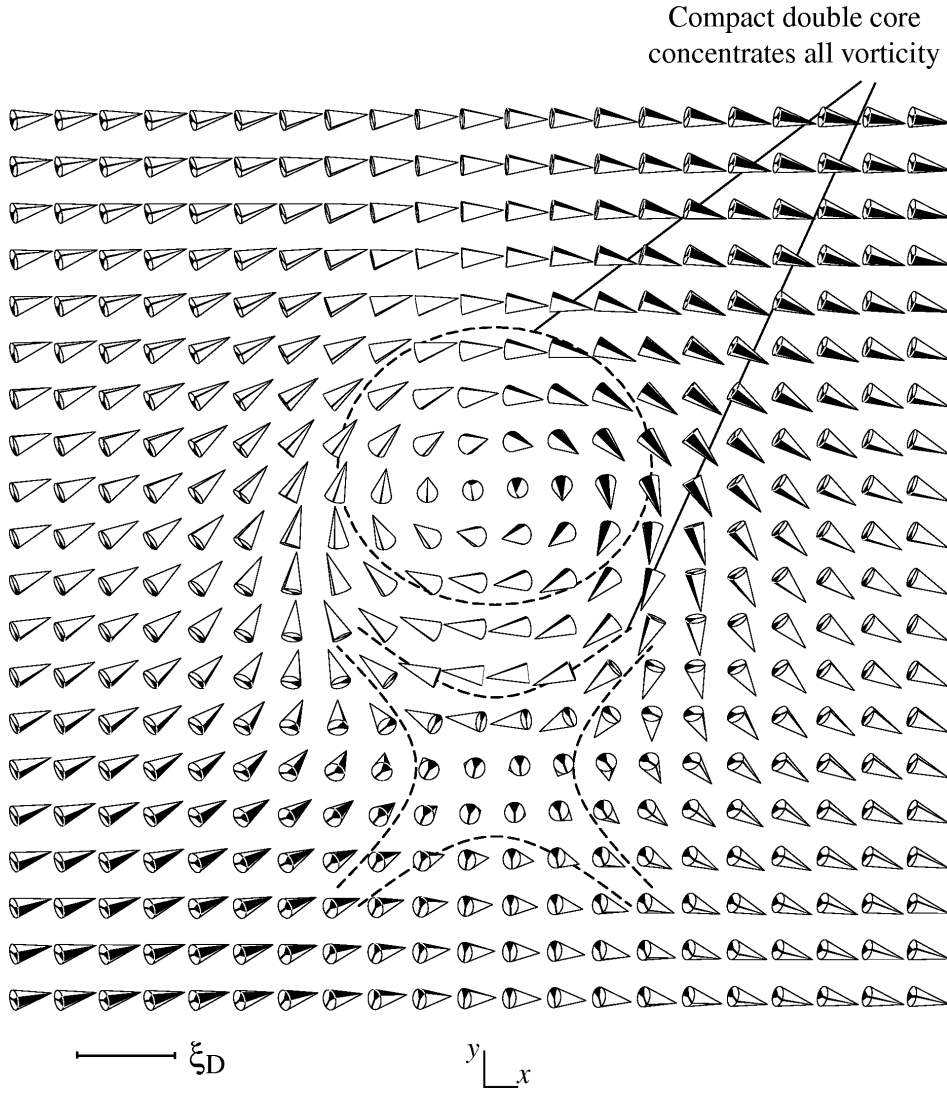


Figure 8. Dipole-unlocked orbital $\hat{\ell}$ texture in the soft core of the doubly-quantized high-field vortex in $^3\text{He-A}$.

$\hat{\mathbf{n}}$ around $\hat{\ell}$ when one makes one full circle along the outer edge of the figure: Two full 2π rotations are performed, which means that the superfluid circulation trapped around the soft core corresponds to 2 quanta. The spin anisotropy axis $\hat{\mathbf{d}}$ is oriented along $\hat{\mathbf{x}}$ outside the soft core and is deflected only little from this orientation within the core. Thus the magnetic anisotropy energy is almost entirely minimized. The radius of the soft core

is seen to be approximately $3\xi_D$, when compared to the yardstick on the bottom of the figure. It is determined by the balance of the kinetic flow energy outside the core and the spin-orbit energy within the core, since the total gradient energy in the core is roughly independent of the core size. The nonaxisymmetric structure has the consequence that the triangular elementary lattice cell is not exactly of the ideal hexagonal form, but elongated by several percent along \hat{y} (ie. the direction connecting the centers of the Mermin-Ho vortices).

The doubly-quantized vortex is generally always formed when rotation is started at slow angular acceleration in a magnetic field, if the liquid is already in the A phase state. Only the vortex sheet has a lower critical velocity, but it is not formed if a splay soliton sheet is not present and if Ω is slowly and monotonically increased.

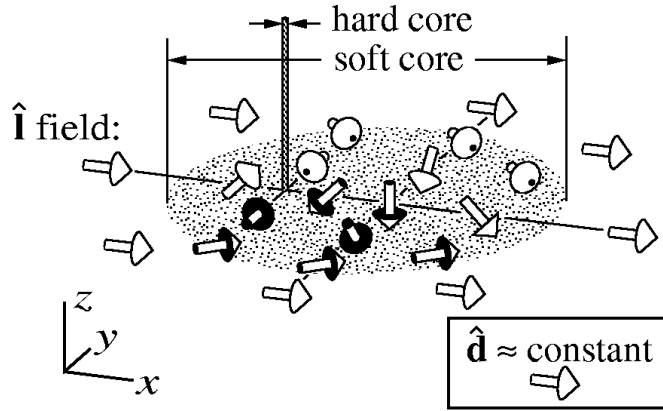


Figure 9. Sketch of the dipole-unlocked ℓ texture in the soft core of the singly quantized vortex in $^3\text{He-A}$.

Figure 9. The dipole-unlocked soft core of the singly quantized vortex in $^3\text{He-A}$ [18, 13] includes also a singular hard core, where the order parameter amplitude deviates from the A phase form. As in Fig. 2, the radius of the hard core is on the order of the superfluid coherence length ξ and orders of magnitude smaller than that of the soft core. A singly quantized vortex provides a smoother coverage of vorticity and thus a lower value in the hydrodynamic flow contribution. This property makes the singly quantized vortex preferable at low Ω (below 1 rad/s). However, as discussed in the context of Fig. 4, except very close to T_c , the critical velocity for creating the singular core is much larger than that needed to form a singularity-free structure and thus singular vortices are not created at temperatures below T_c .

A singly quantized vortex in A phase could in principle have the structure of a simple phase vortex, like in ^4He or $^3\text{He-B}$, with $\hat{\mathbf{d}} = \hat{\ell}$ in the transverse plane ($\perp \mathbf{H}, \vec{\Omega}$) everywhere else except at the hard core where the order parameter changes form. However, textural energy considerations show that a lower energy configuration is obtained by surrounding the hard core with a dipole-unlocked soft core. In this situation the vortex still looks like a phase vortex from outside the soft core, with $\hat{\ell} = \hat{\mathbf{d}} = \text{hat}\mathbf{x}$, and $\hat{\mathbf{m}} + i\hat{\mathbf{n}}$ rotating about $\hat{\ell}$ by 2π on encircling the soft core once. This configuration thus has trapped one quantum of circulation around the soft core.

Within the soft core the orbital triad rotates around $\hat{\mathbf{n}}$ by about 90° on moving from the perimeter to the hard core. At the hard core one then finds that $\hat{\ell}$ rotates by 2π about $\hat{\mathbf{m}}$ when one moves around the core, or that the polar angle β of $\hat{\ell}$ changes by 2π . This means that there is no circulation about the hard core and the vorticity vanishes: $\vec{\nabla} \times \mathbf{v}_s = \sin\beta (\vec{\nabla}\beta \times \vec{\nabla}\alpha) = 0$, as the azimuthal angle α remains constant. The hard core is a pure disgyration line, all circulation arises from the soft core with its 2π distribution of $\hat{\ell}$ orientations, and v_s goes smoothly to zero on approaching the hard core. Such a structure makes the soft core nonaxisymmetric, the hard core lies slightly displaced from the geometric center of the soft core, and the lattice is distorted from the ideal hcp structure.

Figure 10. In the ^3He literature planar structures are called solitons. In a magnetic field ($H > H_D$) stationary solitons are localized and topologically stable dipole-unlocked structures [19]. Such a soliton sheet separates two regions with degenerate $\hat{\ell}$ textures: On one side of the sheet $\hat{\ell}$ is aligned parallel to $\hat{\mathbf{d}}$ while on the other side $\hat{\ell}$ and $\hat{\mathbf{d}}$ are antiparallel. The reorientation across the wall is primarily the responsibility of the $\hat{\ell}$ vector. Nevertheless, these sheets are called composite solitons since the orientation of $\hat{\mathbf{d}}$ also changes across the soliton: It participates in the reorientation process by performing approximately $\frac{1}{5}$ of the change. In the simple case of zero flow both $\hat{\mathbf{d}}$ and $\hat{\ell}$ are confined in the plane $\perp \mathbf{H}$ also within the soliton.

In the cylindrical container two soliton structures are of particular interest: The transverse soliton appears as a plane perpendicular to the symmetry axis of the cylinder. In an axially oriented field it has *twist* structure. The longitudinal soliton is oriented along the cylinder axis and has *splay* structure in the axial field. Since $\hat{\mathbf{d}}$ is confined to the transverse plane independently of the soliton orientation, both structures preserve $\ell_z = 0$ also within the soliton sheet. In the twist soliton the $\hat{\ell}$ orientation is twisted around as a function of z while traversing across the sheet along $\hat{\mathbf{z}}$. In the splay structure the reorientation of $\hat{\ell}$ occurs at constant z within one and the same transverse plane.

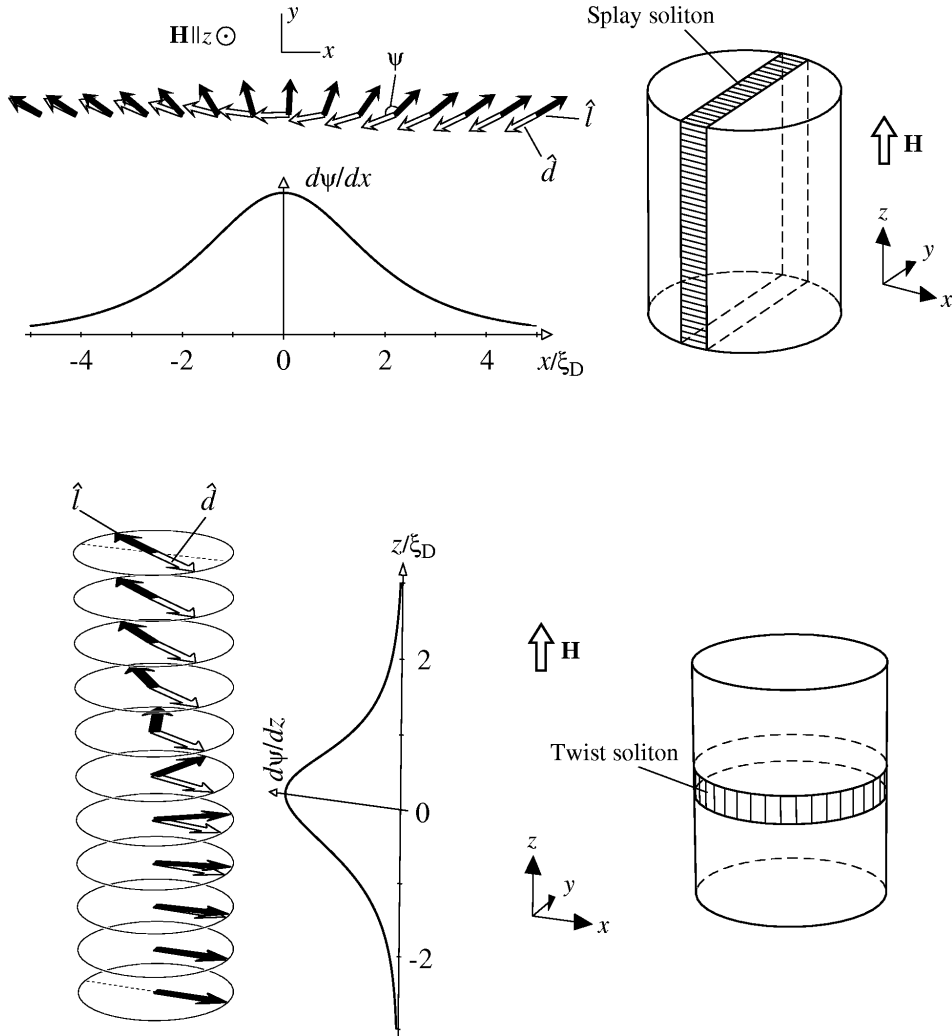


Figure 10. Topological soliton sheets in the $\hat{\ell}$ texture of $^3\text{He-A}$.

Both structures are modified by counterflow, when rotation is started. Since $\hat{\ell}$ is aligned either parallel or antiparallel by the counterflow, initially the width of the transverse soliton is compressed. Furthermore, within the soliton the critical velocity for the creation of the doubly-quantized singularity-free vortex line (Fig. 8) drops typically by a factor of 3 from that in the bulk outside the soliton [16]. Thus vortex lines are created at low rotation velocity. These tend to destabilize the presence of a transverse soliton sheet within the cylinder such that it is pushed either to the top or bottom wall and annihilated there.

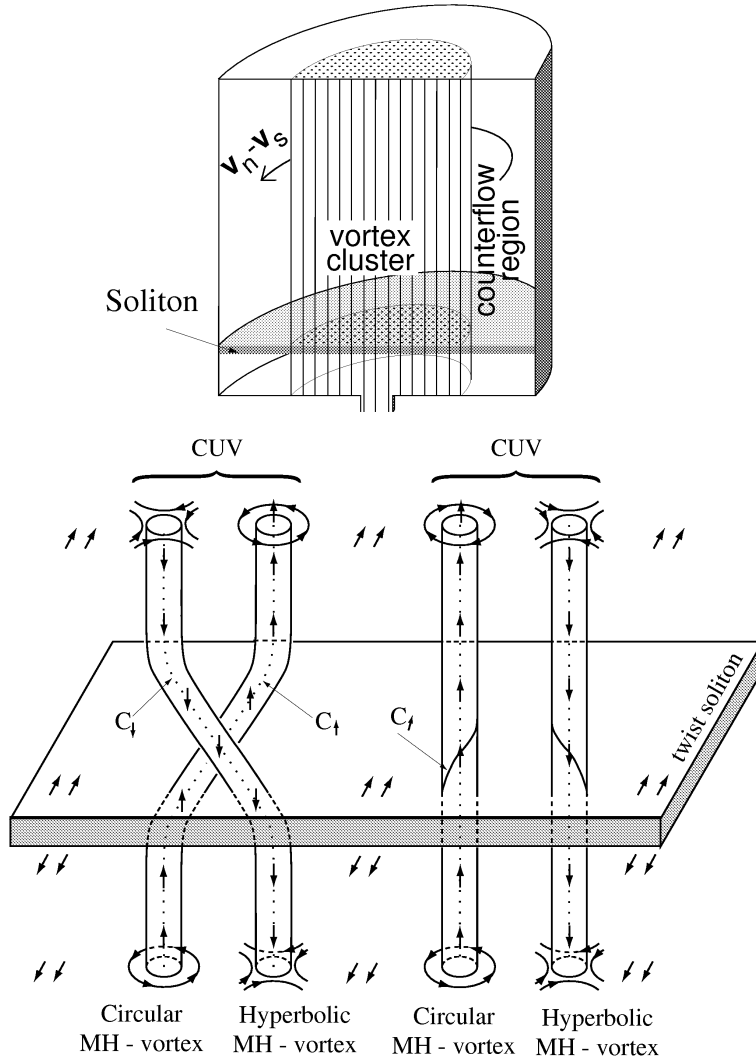


Figure 11. Intersection of the doubly-quantized singularity-free vortex line with a transverse soliton in $^3\text{He-A}$.

In contrast, the longitudinal soliton sheet is oriented perpendicular to the counterflow direction. It becomes unstable with respect to the creation of vorticity at essentially zero critical velocity and the vortex sheet (Fig. 12) starts to develop [20]. Thus the splay soliton, by transforming into the vortex sheet, is stabilized by rotation.

Transverse solitons usually appear during a rapid cool down through T_c , when the container is not rotating. In a long cylinder several transverse soliton sheets can then be stacked one on top of the other in a long-lived

unstable state of metastability. During rapid rotational acceleration they can pairwise combine and annihilate each other or they can be swept to the top or bottom walls of the cylinder. The longitudinal soliton is only infrequently found after a rapid cool down through T_c (at $\Omega = 0$), since its stability in the cylinder is most fragile.

Figure 11. The intersection of the doubly-quantized singularity-free vortex line with a transverse twist soliton is a continuous point-like $\hat{\ell}$ texture. It belongs to the π_3 homotopy group and is created when a line defect of π_2 topology crosses a planar π_1 defect. Although the $\hat{\ell}$ texture in this knot-like structure has not been directly mapped by the experiment, its existence must be inferred from the measurements and in this sense it represents the first experimentally verified point-like structure in the ^3He superfluids. The intersection can be maintained in a state of unstable balance in the rotating cylinder at a relatively low density of vortex lines ($\Omega \lesssim 0.3$ rad/s).

There are two possible configurations in which the knot can appear: The circular and hyperbolic Mermin-Ho vortices, the two constituents of the doubly-quantized vortex (Fig. 8), may interchange places and form a tangled intersection within the soliton plane (*on the left*). In this case the Mermin-Ho vortices remain continuous across the soliton plane. Since the $\hat{\ell}$ orientation is also changed by 180° across the soliton, this intersection leaves the $\hat{\ell}$ texture of the doubly-quantized vortex line in Fig. 8 unchanged.

In the second case (*on the right*) the Mermin-Ho vortices do not change places, but each of them is twisted separately while crossing the soliton. Here the doubly-quantized vortices on the two sides of the soliton plane become mirror images of each other. At present time it is not known which one of these two intersections represents the lower textural energy state.

Figure 12. The dipole-unlocked vortex sheet in $^3\text{He-A}$ [20] is a combined object which is made up of a longitudinal planar soliton (Fig. 10) and the two linear Mermin-Ho vortices (Fig. 7). Within the sheet the two types of Mermin-Ho vortices, the circular and the hyperbolic vortex, are stacked one after the other as an alternating chain. At any reasonable value of Ω the vorticity becomes evenly distributed along the sheet: On moving in the x direction along the centerline of the sheet, it is seen that $\hat{\ell}$ is winding around the x axis at uniform pitch.

Another important characteristic is the alternating pattern of bend and twist sections. In the bend section $\hat{\ell}$ rotates by 180° while confined in the same transverse plane at constant z , whereas in the twist section $\hat{\ell}$ is rotated around the y axis by 180° . Outside the sheet $\hat{\ell}$ and the local counterflow $\mathbf{v} = \mathbf{v}_s - \mathbf{v}_n$ are oriented parallel to the sheet, but on opposite sides this orientation is reversed by 180° . Across the sheet the velocity changes in magnitude due to the vorticity contained in the sheet. The overall config-

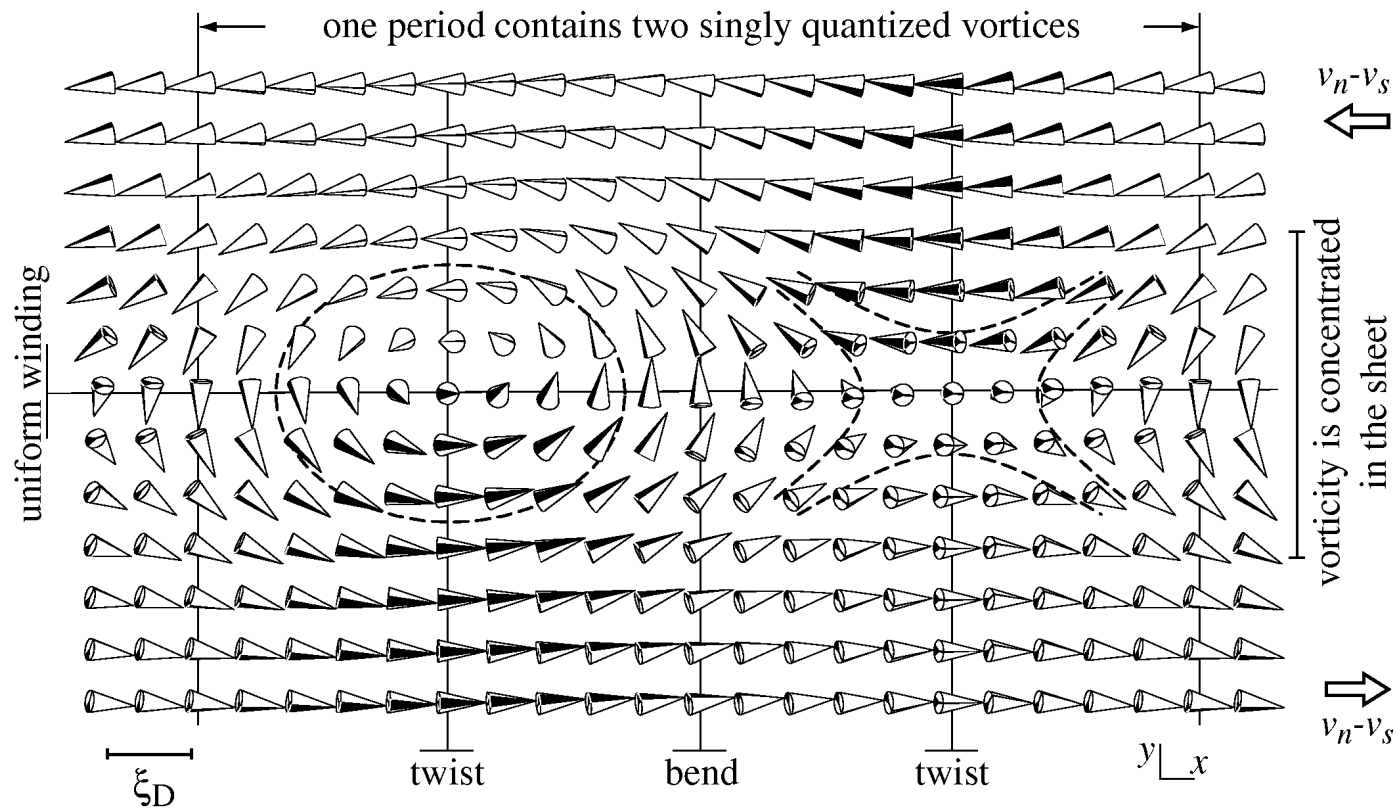


Figure 12. Dipole-unlocked orbital texture of the vortex sheet in $^3\text{He-A}$.

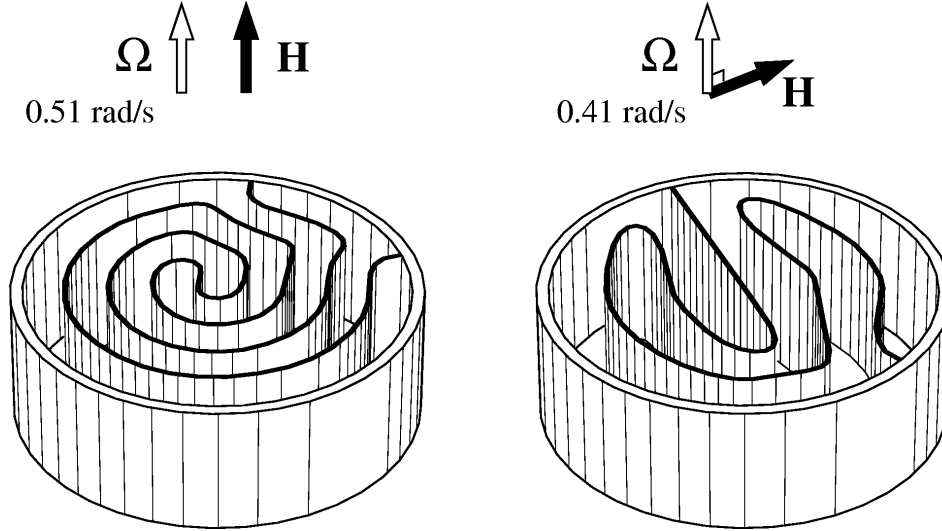


Figure 13. Folding configurations of the vortex sheet in a rotating container with ${}^3\text{He-A}$.

uration of the vortex sheet in the rotating container consists of parallel layers of vorticity (Fig. 13), separated by irrotational counterflow. This hydrodynamic structure was first discussed by Landau and Lifshitz [21].

Figure 13. In the equilibrium state the vortex sheet forms a continuous meander which has two connection lines with the lateral cylinder wall. Vorticity enters and leaves the sheet at these connection lines. The meandering sheet fills the rotating container evenly with equidistant folds. Their spacing is determined by the balance of the sheet's surface tension σ and the kinetic energy of the counterflow: $b = [3\sigma/(\rho_{s\parallel} \Omega^2)]^{1/3}$. Thus with increasing rotation velocity the length of the sheet is extended $\propto \Omega^{2/3}$ and the number of folded layers increases.

The spacing b of the folds and the periodicity p within the sheet have to fulfill the requirement of solid-body rotation on a radial length scale $\gg b$, so that the large-scale average of the counterflow velocity becomes $\langle \mathbf{v} \rangle = \vec{\Omega} \times \mathbf{r}$. This condition gives the usual equilibrium density of vorticity: $\kappa/bp = |\vec{\nabla} \times \mathbf{v}| = 2\Omega$, where $\kappa = 2\kappa_0 = h/m_3$ is the circulation of one elementary unit with the two Mermin-Ho vortices. Although $b > p$, roughly speaking b and p are comparable to the intervortex distance in a vortex array consisting of doubly-quantized vortex lines. This means that p is larger than the distance between the two Mermin-Ho constituents within one doubly quantized vortex. Due to this distributed structure, at higher rotation velocities the vortex sheet becomes an economic arrangement of quantized vorticity. Although not yet confirmed by measurement, numeric

minimization of the textural energies suggests that at $\Omega > 3$ rad/s the vortex sheet becomes the equilibrium form of vorticity [13].

The arrangement of the folds depends on the direction of the applied magnetic field. In an axially oriented field a more symmetric configuration evolves, which resembles a double spiral of coaxial sheets. In the transverse field $\hat{\mathbf{d}}$ is confined in the transverse plane to the orientation perpendicular to the field. To minimize dipole coupling, $\hat{\ell}$ attempts to align itself parallel to $\hat{\mathbf{d}}$ in much of the container and therefore the folds prefer to form parallel walls perpendicular to \mathbf{H} . If the field is rotated to a new orientation after forming the vortex sheet, frustrated and distorted folding patterns are created.

An important property of the vortex sheet is its low critical velocity. If the rotation velocity is increased above the equilibrium value, a macroscopic counterflow forms which encircles the vortex sheet next to the container wall. It compresses the vorticity towards the center of the container and thereby leaves the two regions of the soliton sheet at the contact lines devoid of vorticity. In these two regions the flow crosses the soliton sheet and the critical velocity is substantially reduced.

The low critical velocity at the connection lines makes the vortex sheet the dominating form of vorticity as soon as the longitudinal soliton is present. In rapidly changing rotation the vortex sheet generally also dominates the creation and annihilation of vorticity. This is caused by the fact that the vortex sheet has the fastest dynamic response for minimizing the dominant energy contribution, the kinetic energy of the macroscopic counterflow $\sim \frac{1}{2}\rho_{s\parallel}(v_s - v_n)^2$, where $\rho_{s\parallel}$ is the density of the superfluid component. Consequently more often than not, the vortex sheet is the regnant form of vorticity in the rotating container.

References

1. Due to space considerations figures are of reduced quality. Full quality figures are available from <ftp://boojum.hut.fi/pub/publications/lowtemp/LexTopDef/>
2. Also at Kapitza Institute for Physical Problems, ul. Kosygina 2, 117334 Moscow, Russia.
3. D. Vollhardt and P. Wölfle, *The superfluid phases of helium 3* (Taylor & Francis, London, 1990).
4. G.E. Volovik, *Exotic properties of superfluid ^3He* (World Scientific Publishing Co., Singapore, 1992); M.M. Salomaa and G.E. Volovik, *Rev. Mod. Phys.* **59**, 533 (1988); A.L. Fetter, in *Prog. Low Temp. Phys.*, Vol X, p. 1, (Elsevier Science Publ., Amsterdam, 1986).
5. G.E. Volovik, *Physica B* **255**, 86 (1998); V.B. Eltsov, M. Krusius, and G.E. Volovik, *preprint* (<http://xxx.lanl.gov/abs/cond-mat/9809125>).
6. O.V. Lounasmaa and E.V. Thuneberg, *Proc. Natl. Acad. Sci. USA* **96**, 7760 (1999).
7. O.T. Ikkala, G.E. Volovik, P.J. Hakonen, Yu.M. Bunkov, S.T. Islander, and G.A. Kharadze, *Pis'ma Zh. Eksp. Teor. Fiz.* **35**, 338 (1982) [*JETP Lett.* **35**, 416 (1982)]; P.J. Hakonen, O.T. Ikkala, S.T. Islander, O.V. Lounasmaa, and G.E. Volovik, *J. Low Temp. Phys.* **53**, 425 (1983).

8. E.V. Thuneberg, *Phys. Rev. Lett.* **56**, 359 (1986); *Phys. Rev. B* **36**, 3583 (1987).
9. Y. Kondo, J.S. Korhonen, M. Krusius, V.V. Dmitriev, Yu.M. Mukharsky, E.B. Sonin, and G.E. Volovik, *Phys. Rev. Lett.* **67**, 81 (1991).
10. Y. Kondo, J.S. Korhonen, M. Krusius, V.V. Dmitriev, E.V. Thuneberg, and G.E. Volovik, *Phys. Rev. Lett.* **68**, 3331 (1992); J.S. Korhonen, Y. Kondo, M. Krusius, E.V. Thuneberg, and G.E. Volovik, *Phys. Rev. B* **47**, 8868 (1993-II).
11. M. Krusius, E.V. Thuneberg, and Ü. Parts, *Physica B* **197**, 376 (1994).
12. Ü. Parts, J.M. Karimäki, J.H. Koivuniemi, M. Krusius, V.M. Ruutu, E.V. Thuneberg, and G.E. Volovik, *Phys. Rev. Lett* **75**, 3320 (1995).
13. J.M. Karimäki and E.V. Thuneberg, *Phys. Rev. B*, in press (<http://xxx.lanl.gov/abs/cond-mat/9902207>).
14. J.P. Pekola, K. Torizuka, A.J. Manninen, J.M. Kynäräinen, and G.E. Volovik, *Phys. Rev. Lett.* **65**, 3293 (1990).
15. V.M. Ruutu, Ü. Parts, and M. Krusius, *J. Low Temp. Phys.* **103**, 331 (1996).
16. V.M. Ruutu, J. Kopu, M. Krusius, Ü. Parts, B. Plaçais, E.V. Thuneberg, and W. Xu, *Phys. Rev. Lett.* **79**, 5058 (1997).
17. M. Nakahara, T. Ohmi, T. Tsuneto, and T. Fujita, *Prog. Theor. Phys.* **62**, 874 (1979); *ibid.* **60**, 671 (1978).
18. H.K. Seppälä and G.E. Volovik, *J. Low Temp. Phys.* **51**, 279 (1983); X. Zotos and K. Maki, *Phys. Rev. B* **30**, 145 (1984); V.Z. Vulovic, D.L. Stein, and A.L. Fetter, *Phys. Rev. B* **29**, 6090 (1984); T. Ohmi, *J. Low Temp. Phys.* **56**, 183 (1984); H.K. Seppälä, P.J. Hakonen, M. Krusius, T. Ohmi, M.M. Salomaa, J.T. Simola, and G.E. Volovik, *Phys. Rev. Lett.* **52**, 1802 (1984); P.J. Hakonen, M. Krusius, and H.K. Seppälä, *J. Low Temp. Phys.* **60**, 187 (1985).
19. K. Maki and P. Kumar, *Phys. Rev. Lett* **38**, 557 (1977); *Phys. Rev. B* **16**, 182 (1977); D. Vollhardt and K. Maki, *Phys. Rev. B* **20**, 963 (1979); R. Hänninen and E.V. Thuneberg, to be published.
20. Ü. Parts, E.V. Thuneberg, G.E. Volovik, J.H. Koivuniemi, V.H. Ruutu, M. Heinilä, J.M. Karimäki, and M. Krusius, *Phys. Rev. Lett* **72**, 3839 (1994); E.V. Thuneberg, *Physica B* **210**, 287 (1995); M.T. Heinilä and G.E. Volovik, *Physica B* **210**, 300 (1995); Ü. Parts, V.M. Ruutu, J.H. Koivuniemi, M. Krusius, E.V. Thuneberg, and G.E. Volovik, *Physica B* **210**, 311 (1995).
21. L. Landau and E. Lifshitz, *Dokl. Akad. Nauk.* **100**, 669 (1955).
22. V.M. Ruutu, Ü. Parts, J.H. Koivuniemi, M. Krusius, E.V. Thuneberg, and G.E. Volovik, *Pis'ma Zh. Eksp. Teor. Fiz.* **60**, 659 (1994).